Two-dimensional problem of an infinite matrix reinforced with a Steigmann-Ogden cylindrical surface of circular arc cross-section

Zhilin Han[a], Anna Y. Zemlyanova[b], Sofia G. Mogilevskaya[c,*]

[a] *College of Science, Donghua University, Shanghai, 201620, China*
[b] *Department of Mathematics, Kansas State University, 138 Cardwell Hall, Manhattan, Kansas, 66506, USA*
[c] *Department of Civil, Environmental, and Geo- Engineering, University of Minnesota, 500 Pillsbury Drive S.E., Minneapolis, MN, 55455, USA*

Abstract

The plane strain problem of an elastic matrix subjected to uniform far-field load and containing a Steigmann-Ogden material surface with circular arc cross-section is considered. The governing equations and the boundary conditions for the problem are reviewed. Exact complex integral representations for the elastic fields everywhere in the material are provided. The problem is further reduced to the system of real variables hypersingular boundary integral equations in terms of the unknown strain component of the surface stress tensor and the unknown linear combination involving the rotational component and its second derivative, and various problem parameters. The two unknowns are then approximated by the series of trigonometric functions that are multiplied by the square root weight functions to allow for automatic incorporation of the tip conditions. The unknown coefficients in series are found from the system of linear algebraic equations that is solved using standard collocation method. The numerical examples are presented to illustrate the influence of dimensionless parameters. The connection of the problem with that of rigid circular arc is discussed.

Keywords: Composites with ultra thin and stiff reinforcements, Steigmann-Ogden theory, Gurtin-Murdoch theory, Elastic potentials, Boundary integral equations

*Corresponding author
Email addresses: hanzhilin@dhu.edu.cn (Zhilin Han), azem@ksu.edu (Anna Y. Zemlyanova), mogil003@umn.edu (Sofia G. Mogilevskaya)

1. Introduction

In this paper, we consider the plane strain problem of an infinite isotropic elastic matrix that contains a Steigmann-Ogden material surface (see Steigmann and Ogden (1999, 1997)) with circular arc cross-section and subjected to uniform far-field load. The surface represents a shell of vanishing thickness that is characterized by its own elastic and bending stiffnesses and the residual surface tension. The problem has applications in the area of modeling composite materials that use ultra-thin stiff reinforcements, e.g., Cao (2014), Güler and Bağcı (2020), Papageorgiou et al. (2017, 2020), Suk et al. (2010), Mirzaei and Abbasi (2023).

In recent publications, several solutions were proposed for the two-dimensional problems involving Gurtin-Murdoch (Gurtin and Murdoch (1975, 1978)) and Steigmann-Ogden material surfaces along a straight segment, see e.g. Baranova et al. (2020), Mogilevskaya et al. (2021b), Zemlyanova et al. (2023), Zemlyanova (2023). The first numerical algorithm for solving the plane-strain problem involving a Gurtin-Murdoch curve along a circular arc was proposed in Han et al. (2023). In all above mentioned publications, the solutions were obtained using the theories of elastic layer potentials and integral equations. In the solution process, the problems were reduced to the solutions of the systems of real variables hypersingular boundary integral equations in terms of the strain and rotation components of the surface stress tensor. The equations were decoupled for the case of a surface along a straight segment, while the equations for the circular arc were coupled. In the case of a material surface along a straight segment and zero surface tension, it was demonstrated in Mogilevskaya et al. (2021b), Zemlyanova et al. (2023) that the case of rigid line inclusion, see e.g. Ballarini (1987), Corso et al. (2008), Goudarzi et al. (2020), Markenscoff et al. (1994), Wang et al. (1985), could be recovered by proper choice of surface elastic parameters. This was not the case for the problem involving Gurtin-Murdoch's circular arc surface, as in Han et al. (2023) it was shown that the latter problem was not reducible to that of a rigid arc, see Liu and Jiang (1994), even when the arc's elastic parameters were chosen to be the same

as for the corresponding straight line case.

In the present paper, we derive, for the first time, numerical solution of the two-dimensional plane strain problem that involves a Steigmann-Ogden circular arc surface. Here too, we employ the theories of elastic layer potentials and integral equations. However, unlike in the case of Gurtin-Murdoch circular arc surface, the boundary integral equations for the Steigmann-Ogden surface contain not only the strain and rotational components of surface stress tensor but the linear combination of the latter component and its second derivative. Depending on the parameters involved, three different options exist to find analytical expression for the rotational component via that combination. After that is done, the problem is reduced to the solution of the systems of coupled real variables hypersingular boundary integral equations in terms of the surface stress (that is expressed via the strain component) and the above mentioned combination for the rotational component. The combination and the surface stress are approximated by the truncated series of trigonometric functions multiplied by the square root weight functions. The system of linear algebraic equations for the unknown series coefficients is obtained by using standard collocation method. The elastic fields in the matrix are then found using appropriate complex integral representations. The obtained solution is used to illustrate the influence of governing dimensionless parameters. As in Han et al. (2023), we study the connection of our solution with that for the rigid arc case.

The paper is structured as follows. In Section 2, we formulate the problem under study and review the governing equations of the Steigmann-Ogden theory. In Section 3, we list the exact complex variables integral representations for the fields, and present the governing complex variable boundary integral equation. In Section 4, we reduce the latter equation to the system of real variables boundary integral equations and, after introducing the dimensionless parameters, reformulate the system in dimensionless settings. In Section 5, we describe major steps of the proposed numerical algorithm. In Section 6, we discuss the con-

nection of our solution with that for the rigid arc case. Section 7 contains several examples of numerical simulations. Concluding remarks are presented in Section 8.

2. Problem formulation and governing equations of the Steigmann-Ogden theory

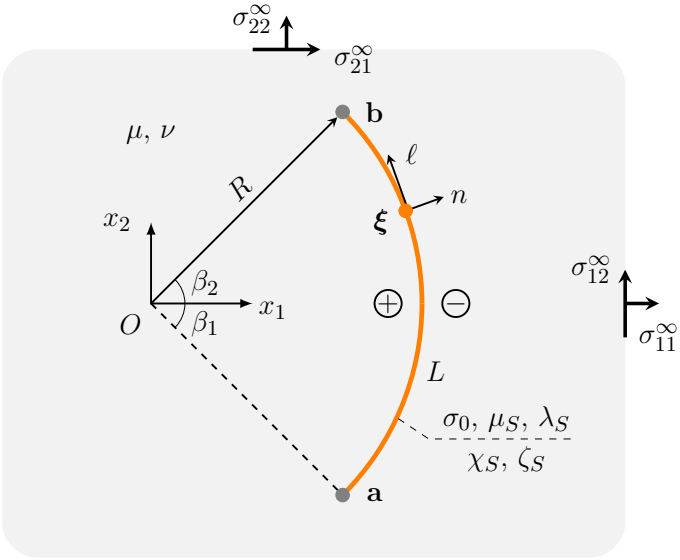

Figure 1: Problem configuration: a Steigmann-Ogden circular arc in an elastic matrix

Consider the plane strain problem of an infinite isotropic elastic matrix that contains a cross-section of a Steigmann-Ogden material surface that represents the circular arc L of radius R with the tips at the points $\boldsymbol{\xi} = \mathbf{a}$, $\boldsymbol{\xi} = \mathbf{b}$, see Fig. 1. The matrix, characterized by the shear modulus μ and Poisson's ratio ν, is subjected to the uniform far-field load σ_{11}^{∞}, σ_{22}^{∞}, σ_{12}^{∞}, where $\sigma_{12}^{\infty} = \sigma_{21}^{\infty}$. The origin of the global Cartesian coordinate system is chosen to be located at the center of the circle on which arc is located. Additionally, the local coordinate system with the mutually orthogonal unit vectors $\boldsymbol{n}$, $\boldsymbol{\ell}$ is introduced and the notations "+" ("−") identify the regions located from the left (right) of $\boldsymbol{n}$, as shown on Fig. 1.

According to the Steigmann-Ogden theory, it is assumed that L is characterized by its own elastic stiffness parameters μ_S, λ_S, bending stiffness parameters χ_S, ζ_S, and by the residual surface tension σ_0. The governing equations for the theory include the standard

Navier equation for the displacements inside the matrix supplemented by the conditions across L and at its tips. The supplemental conditions for the problem under study can be deduced from the corresponding conditions for a curve of an arbitrary sufficiently smooth shape reported in Mogilevskaya et al. (2021b), Zemlyanova et al. (2023), Han et al. (2023), see also a review in Mogilevskaya et al. (2021a), by assuming that the local radius of curvature $R = R(s)$ on L is constant.

Thus, the conditions for the fields across L at the point $\boldsymbol{\xi} \in L$ (here and below we omitted the argument $\boldsymbol{\xi}$ for brevity) are

$$u_1^+ = u_1^- = u_1, \;\; u_2^+ = u_2^- = u_2, \tag{1}$$

$$\Delta\sigma_n = \sigma_n^+ - \sigma_n^- = -\frac{\sigma^S}{R} + \sigma_0 \frac{\partial \omega^S}{\partial s} - (2\chi_S + \zeta_S)\frac{\partial^3 \omega^S}{\partial s^3}, \tag{2}$$

$$\Delta\sigma_\ell = \sigma_\ell^+ - \sigma_\ell^- = \frac{\partial \sigma^S}{\partial s} + \sigma_0 \frac{\omega^S}{R} - \frac{2\chi_S + \zeta_S}{R}\frac{\partial^2 \omega^S}{\partial s^2}, \tag{3}$$

where u_1 and u_2 are the displacement components of the bulk material in the global coordinate system, σ_n and σ_ℓ are the corresponding normal and shear tractions, and s is the arc length. The superscripts "+", "−" here and below describe the limit values of the fields when L is approached from the direction of that of the normal vector or from the opposite direction, respectively. The expressions for the surface stress σ^S, surface strain ε^S, and surface rotation ω^S involved in Eqs. (2)-(3) are

$$\sigma^S = \sigma_0 + (\lambda_S + 2\mu_S)\varepsilon^S, \tag{4a}$$

$$\varepsilon^S = \frac{u_n}{R} + \frac{\partial u_\ell}{\partial s}, \tag{4b}$$

$$\omega^S = -\frac{u_\ell}{R} + \frac{\partial u_n}{\partial s}, \tag{4c}$$

in which u_n and u_ℓ are the normal and shear components of the displacements. Note that

for the case of vanishing bending parameters, the jump conditions of Eqs. (2)-(3) reduce to those for the Gurtin-Murdoch model.

The conditions at the tips $\boldsymbol{\xi} = \mathbf{a}$ and $\boldsymbol{\xi} = \mathbf{b}$ of L for the Steigmann-Ogden model are given by the following equations:

$$\sigma^S = 0, \tag{5a}$$

$$(2\chi_S + \zeta_S)\frac{\partial \omega^S}{\partial s} = 0, \tag{5b}$$

$$\sigma_0 \omega^S - (2\chi_S + \zeta_S)\frac{\partial^2 \omega^S}{\partial s^2} = 0. \tag{5c}$$

For comparison, we also list the tip conditions for the Gurtin-Murdoch model (Mogilevskaya et al. (2021b), Zemlyanova et al. (2023), Han et al. (2023)). They are

$$\sigma^S = 0, \tag{6a}$$

$$\sigma_0 \omega^S = 0. \tag{6b}$$

Compared with Eqs. (6), the tip conditions for the Steigmann-Ogden model of Eqs. (5) have extra terms that involve the combination of the bending parameters and the derivatives of function ω^S. Here too, Eqs. (5) formally reduces to Eqs. (6) if $2\chi_S + \zeta_S = 0$. However, we emphasize that, when the surface tension vanishes, the two models represent two different interface regimes, with Gurtin-Murdoch model representing the limiting case of the so-called membrane interphase, while the Steigmann-Ogden model that of the inextensible shell interphase, see Benveniste and Miloh (2001).

3. Governing integral representations

The integral representations for the elastic fields in the material system under study can be deduced from the representations for more general case of a curve of an arbitrary shape,

see Linkov and Mogilevskaya (1998), Mogilevskaya and Linkov (1998), Mogilevskaya et al. (2021a,b), Zemlyanova et al. (2023), Han et al. (2023).

The representation for the complex displacements $u = u_1 + \mathrm{i}u_2$ outside of L is

$$u(z) = u^{\infty}(z) - \frac{1}{4\pi \mathrm{i}\mu(\kappa+1)} \left\{ \int_L \Delta\sigma(\tau) \left[2\kappa \ln(z-\tau) - \kappa K_1(\tau, z)\right] \mathrm{d}\tau + \int_L \overline{\Delta\sigma(\tau)} K_2(\tau, z)\, \mathrm{d}\overline{\tau} \right\}, \tag{7}$$

while the derivative of Eq. (7) on the curve on which the point z is located, as in Mogilevskaya et al. (2021b), Zemlyanova et al. (2023), Han et al. (2023), is given by

$$u'(z) = [u^{\infty}(z)]' + \frac{1}{4\pi \mathrm{i}\mu(\kappa+1)} \left\{ \int_L \Delta\sigma(\tau) \left[2\kappa \frac{1}{\tau - z} + \kappa \frac{\partial}{\partial z} K_1(\tau, z)\right] \mathrm{d}\tau - \int_L \overline{\Delta\sigma(\tau)} \frac{\partial}{\partial z} K_2(\tau, z)\, \mathrm{d}\overline{\tau} \right\}, \tag{8}$$

in which $u'(z) = \partial u/\partial z + (\partial u/\partial \overline{z})(\partial \overline{z}/\partial z)$.

In Eq. (7) and Eq. (8), i is imaginary unit with $\mathrm{i}^2 = -1$, $z = x_1 + \mathrm{i}x_2$ is the complex combination of the Cartesian coordinates of the point $z \notin L$, $\tau = \tau_1 + \mathrm{i}\tau_2 \in L$, $\Delta\sigma = \Delta\sigma_n + \mathrm{i}\Delta\sigma_\ell$. $\kappa = 3 - 4\nu$, $K_1(\tau, z) = \ln[(\tau - z)/(\overline{\tau} - \overline{z})]$, $K_2(\tau, z) = (\tau - z)/(\overline{\tau} - \overline{z})$, and a bar over a symbol denotes complex conjugation. The expressions for the displacements $u^{\infty}(z)$ and their derivatives $[u^{\infty}(z)]'$ caused by the remote loading are

$$u^{\infty}(z) = \frac{1}{2\mu} \left[(\kappa - 1) \frac{\sigma_{11}^{\infty} + \sigma_{22}^{\infty}}{4} z - \frac{\sigma_{22}^{\infty} - \sigma_{11}^{\infty} - 2\mathrm{i}\sigma_{12}^{\infty}}{2} \overline{z} \right], \tag{9a}$$

$$[u^{\infty}(z)]' = \frac{1}{2\mu} \left[(\kappa - 1) \frac{\sigma_{11}^{\infty} + \sigma_{22}^{\infty}}{4} - \frac{\sigma_{22}^{\infty} - \sigma_{11}^{\infty} - 2\mathrm{i}\sigma_{12}^{\infty}}{2} \frac{\mathrm{d}\overline{z}}{\mathrm{d}z} \right]. \tag{9b}$$

The representation for the complex tractions $\sigma = \sigma_n + \mathrm{i}\sigma_\ell$ on some line outside of L on

which z is located is given by

$$\begin{aligned}\sigma(z) =& \sigma^{\infty}(z) - \frac{1}{2\pi \mathrm{i}(\kappa+1)}\left\{\int_L \Delta\sigma(\tau)\left[(\kappa-1)\frac{1}{\tau-z} + \kappa\frac{\partial}{\partial z}K_1(\tau,z)\right]\mathrm{d}\tau\right. \\ &\left. - \int_L \overline{\Delta\sigma(\tau)}\frac{\partial}{\partial z}K_2(\tau,z)\,\mathrm{d}\bar{\tau}\right\},\end{aligned} \tag{10}$$

in which $\sigma^{\infty}(z)$ can be expressed as

$$\sigma^{\infty}(z) = \frac{\sigma_{11}^{\infty}+\sigma_{22}^{\infty}}{2} + \frac{\sigma_{22}^{\infty}-\sigma_{11}^{\infty}-2\mathrm{i}\sigma_{12}^{\infty}}{2}\frac{\mathrm{d}\bar{z}}{\mathrm{d}z}. \tag{11}$$

Using the limiting procedure in which the field point is allowed to reach some boundary point $\tau^0 = \tau_1^0 + \mathrm{i}\tau_2^0 \in L$ from the direction normal to the boundary at that point, one can obtain the following boundary integral equation, see Mogilevskaya et al. (2021b), Zemlyanova et al. (2023), Han et al. (2023):

$$\begin{aligned}u'(\tau^0) = [u^{\infty}(\tau^0)]' + \frac{1}{4\pi\mathrm{i}\mu(\kappa+1)}&\left\{\fint_L \Delta\sigma(\tau)\left[2\kappa\frac{1}{\tau-\tau^0} + \kappa\frac{\partial}{\partial\tau^0}K_1(\tau,\tau^0)\right]\mathrm{d}\tau\right. \\ &\left. - \int_L \overline{\Delta\sigma(\tau)}\frac{\partial}{\partial\tau^0}K_2(\tau,\tau^0)\mathrm{d}\bar{\tau}\right\}.\end{aligned} \tag{12}$$

Using the equation for the circular arc $\tau\bar{\tau} = R^2$ and the expressions for K_1 and K_2 described previously, we obtain,

$$K_1(\tau,\tau^0) = \ln\frac{(\tau-\tau^0)\tau\tau^0}{R^2(\tau^0-\tau)} = \ln\left(-\frac{\tau\tau^0}{R^2}\right),\ K_2(\tau,\tau^0) = -\frac{\tau\tau^0}{R^2}, \tag{13a}$$

$$\mathrm{d}\bar{\tau} = -\frac{R^2}{\tau^2}\mathrm{d}\tau,\ \frac{\partial K_1}{\partial\tau^0} = \frac{1}{\tau^0},\ \frac{\partial K_2}{\partial\tau^0} = -\frac{\tau}{R^2}. \tag{13b}$$

Substituting the expressions of Eq. (13) into Eq. (12), we obtain the following boundary

integral equation:

$$u'(\tau^0) = u^{\infty}(\tau^0)' + \frac{1}{4\pi \mathrm{i}\mu(\kappa+1)}\left[\fint_L \Delta\sigma(\tau)\left(2\kappa\frac{1}{\tau-\tau^0} + \kappa\frac{1}{\tau^0}\right)\mathrm{d}\tau - \int_L \overline{\Delta\sigma(\tau)}\frac{1}{\tau}\mathrm{d}\tau\right]. \quad (14)$$

4. The system of hypersingular boundary integral equations

4.1. Reduction of Eq. (14) to the system of real variables equations

Using the following representations for the points on L:

$$\tau = Re^{\mathrm{i}\beta},\ \tau^0 = Re^{\mathrm{i}\beta_0},\ \mathrm{d}\tau = \mathrm{i}Re^{\mathrm{i}\beta}\mathrm{d}\beta,\quad \frac{\mathrm{d}\bar{\tau}^0}{\mathrm{d}\tau^0} = \frac{\mathrm{d}}{\mathrm{d}\tau^0}\frac{R^2}{\tau^0} = -e^{-2\mathrm{i}\beta_0}, \quad (15)$$

and substituting Eq. (15) into Eq. (14), we get (here and below, arguments τ^0 and τ are omitted for brevity, unless they are necessary)

$$\begin{aligned} u' = u^{\infty\prime} &+ \frac{\kappa}{2\pi\mu(\kappa+1)}\fint_L (\Delta\sigma_n + \mathrm{i}\Delta\sigma_\ell)\frac{e^{\mathrm{i}\beta}}{e^{\mathrm{i}\beta}-e^{\mathrm{i}\beta_0}}\mathrm{d}\beta \\ &+ \frac{\kappa}{4\pi\mu(\kappa+1)}\fint_L (\Delta\sigma_n + \mathrm{i}\Delta\sigma_\ell)e^{\mathrm{i}(\beta-\beta_0)}\mathrm{d}\beta \\ &- \frac{1}{4\pi\mu(\kappa+1)}\int_L (\Delta\sigma_n - \mathrm{i}\Delta\sigma_\ell)\mathrm{d}\beta. \end{aligned} \quad (16)$$

In the following, we will take into account that the kernels of Eq. (16) can be expressed as

$$\frac{e^{\mathrm{i}\beta}}{e^{\mathrm{i}\beta}-e^{\mathrm{i}\beta_0}} = \frac{1}{2} - \mathrm{i}\frac{\sin(\beta-\beta_0)}{2[1-\cos(\beta-\beta_0)]},\ e^{\mathrm{i}(\beta-\beta_0)} = \cos(\beta-\beta_0) + \mathrm{i}\sin(\beta-\beta_0). \quad (17)$$

One can rewrite Eqs. (4a)-(4c), in complex variables notations as

$$\sigma^S = \sigma_0 + (\lambda_S + 2\mu_S)\varepsilon^S = \sigma_0 + (\lambda_S + 2\mu_S)\,\mathrm{Re}\,u', \quad (18a)$$

$$\varepsilon^S = \frac{u_n}{R} + \frac{\partial u_\ell}{\partial s} = \mathrm{Re}\,u', \quad (18b)$$

$$\omega^S = -\frac{u_\ell}{R} + \frac{\partial u_n}{\partial s} = -\operatorname{Im} u', \tag{18c}$$

where, as before, $u' = \mathrm{d}u/\mathrm{d}\tau + \mathrm{d}u/\mathrm{d}\bar{\tau} \cdot \mathrm{d}\bar{\tau}/\mathrm{d}\tau$.

Using Eqs. (2), (3) and Eqs. (18a) - (18c), boundary integral equation Eq. (16) can be rewritten in terms of σ^S and ω^S. After using integration by parts and implementing the tip conditions of Eq. (5), the final system of boundary integral equations takes the following form:

$$\begin{aligned}
\sigma^S =& \sigma_0 + (\lambda_S + 2\mu_S) \operatorname{Re}(u^\infty)' + \frac{\kappa(\lambda_S + 2\mu_S)}{4\pi R\mu(\kappa+1)} \int_{\beta_1}^{\beta_2} \frac{\sigma^S \cos(\beta - \beta_0)}{1 - \cos(\beta - \beta_0)} \mathrm{d}\beta + \\
& \frac{\kappa(\lambda_S + 2\mu_S)}{4\pi R\mu(\kappa+1)} \int_{\beta_1}^{\beta_2} \left[\sigma_0 \omega^S - (2\chi_S + \zeta_S) \frac{\partial^2 \omega^S}{\partial s^2} \right] \frac{\sin(\beta - \beta_0)}{1 - \cos(\beta - \beta_0)} \mathrm{d}\beta + \\
& \frac{\lambda_S + 2\mu_S}{4\pi R\mu(\kappa+1)} \int_{\beta_1}^{\beta_2} \sigma^S \mathrm{d}\beta,
\end{aligned} \tag{19}$$

$$\begin{aligned}
-\omega^S =& \operatorname{Im}(u^\infty)' - \frac{\kappa}{4\pi R\mu(\kappa+1)} \int_{\beta_1}^{\beta_2} \left[\sigma_0 \omega^S - (2\chi_S + \zeta_S) \frac{\partial^2 \omega^S}{\partial s^2} \right] \frac{\cos(\beta - \beta_0)}{1 - \cos(\beta - \beta_0)} \mathrm{d}\beta + \\
& \frac{\kappa}{4\pi R\mu(\kappa+1)} \int_{\beta_1}^{\beta_2} \frac{\sigma^S \sin(\beta - \beta_0)}{1 - \cos(\beta - \beta_0)} \mathrm{d}\beta + \\
& \frac{1}{4\pi R\mu(\kappa+1)} \int_{\beta_1}^{\beta_2} \left[\sigma_0 \omega^S - (2\chi_S + \zeta_S) \frac{\partial^2 \omega^S}{\partial s^2} \right] \mathrm{d}\beta,
\end{aligned} \tag{20}$$

where β_1 and β_2 are the angles associated with the tips of L and $\operatorname{Re} u^{\infty\prime}$, $\operatorname{Im} u^{\infty\prime}$ are obtained from Eqs. (9b), (15) as

$$\begin{aligned}
\operatorname{Re} u^{\infty\prime} &= \frac{1}{2\mu} \left[(\kappa - 1) \frac{\sigma_{11}^\infty + \sigma_{22}^\infty}{4} - \frac{2\sigma_{12}^\infty \sin(2\beta_0) + \cos(2\beta_0)(\sigma_{11}^\infty - \sigma_{22}^\infty)}{2} \right], \\
\operatorname{Im} u^{\infty\prime} &= \frac{1}{2\mu} \left[\frac{\sigma_{11}^\infty - \sigma_{22}^\infty}{2} \sin(2\beta_0) - \sigma_{12}^\infty \cos(2\beta_0) \right].
\end{aligned} \tag{21}$$

4.2. Dimensionless integral equations

We introduce the following dimensionless parameters:

$$\begin{gathered}
\theta = \beta_2 - \beta_1,\ \tilde{\sigma}_{ij}^\infty = \frac{\sigma_{ij}^\infty}{\mu}, \gamma = \frac{\mu R\theta}{2\mu_S + \lambda_S},\ \tilde{\sigma}^S = \frac{2\sigma^S}{\mu R\theta},\ \tilde{\sigma}_0 = \frac{2\sigma_0}{\mu R\theta},\ \tilde{\delta} = \frac{8(2\chi_S + \zeta_S)}{\mu R^3\theta^3}, \\
\Sigma_1 = 2\operatorname{Re}(u^\infty(\tau^0))',\ \Sigma_2 = \operatorname{Im}(u^\infty(\tau^0))',
\end{gathered} \tag{22}$$

and the new function $z^S(\beta)$ as

$$\tilde{\sigma}_0\omega^S(\beta) - \frac{\theta^2\tilde{\delta}}{4}\frac{\partial^2\omega^S(\beta)}{\partial\beta^2} = z^S(\beta),\ z^S(\beta_1) = z^S(\beta_2) = 0. \tag{23}$$

Substituting Eq. (23) and the parameters of Eq. (22) into Eq. (19) and Eq. (20) , one can rewrite those equations in the dimensionless forms as

$$\begin{aligned}\gamma\tilde{\sigma}^S = \gamma\tilde{\sigma}_0 + \Sigma_1 + \frac{\kappa\theta/2}{2\pi(\kappa+1)}\int_{\beta_1}^{\beta_2}\frac{\tilde{\sigma}^S\cos(\beta-\beta_0) + z^S\sin(\beta-\beta_0)}{1-\cos(\beta-\beta_0)}\mathrm{d}\beta \\ + \frac{\theta/2}{2\pi(\kappa+1)}\int_{\beta_1}^{\beta_2}\tilde{\sigma}^S\mathrm{d}\beta,\end{aligned} \tag{24}$$

$$\begin{aligned}\omega^S = -\Sigma_2 + \frac{\kappa\theta/2}{4\pi(\kappa+1)}\int_{\beta_1}^{\beta_2}\frac{z^S\cos(\beta-\beta_0) - \tilde{\sigma}^S\sin(\beta-\beta_0)}{1-\cos(\beta-\beta_0)}\mathrm{d}\beta \\ - \frac{\theta/2}{4\pi(\kappa+1)}\int_{\beta_1}^{\beta_2} z^S(\beta)\mathrm{d}\beta,\end{aligned} \tag{25}$$

where the unknowns are the functions σ^S, z^S and ω^S. Using Eq. (23) one can obtain the exact relations between z^S and ω^S for the three possible non-trivial cases of $\tilde{\delta} \neq 0$ using the procedure described below.

4.2.1. $\sigma_0 > 0$, $2\chi_S + \zeta_S > 0$

In this case, the general solution of Eq. (23) is

$$\omega^S(\beta) = C_1(\beta)\cosh\left(\frac{2}{\theta}\sqrt{\frac{\tilde{\sigma}_0}{\tilde{\delta}}}\beta\right) + C_2(\beta)\sinh\left(\frac{2}{\theta}\sqrt{\frac{\tilde{\sigma}_0}{\tilde{\delta}}}\beta\right), \tag{26}$$

in which the unknown coefficients $C_1(\beta)$ and $C_2(\beta)$ can be found from standard method of variation of parameters for solving ordinary linear differential equations of the second order.

Using this method, we obtain the following relations:

$$\begin{aligned} C_1'(\beta)\cosh\left(\frac{2}{\theta}\sqrt{\frac{\tilde{\sigma}_0}{\tilde{\delta}}}\beta\right)+C_2'(\beta)\sinh\left(\frac{2}{\theta}\sqrt{\frac{\tilde{\sigma}_0}{\tilde{\delta}}}\beta\right)=0,\\ C_1'(\beta)\frac{2}{\theta}\sqrt{\frac{\tilde{\sigma}_0}{\tilde{\delta}}}\cosh\left(\frac{2}{\theta}\sqrt{\frac{\tilde{\sigma}_0}{\tilde{\delta}}}\beta\right)+C_2'(\beta)\frac{2}{\theta}\sqrt{\frac{\tilde{\sigma}_0}{\tilde{\delta}}}\sinh\left(\frac{2}{\theta}\sqrt{\frac{\tilde{\sigma}_0}{\tilde{\delta}}}\beta\right)=0, \end{aligned} \tag{27}$$

from which, we get

$$\begin{aligned} C_1'(\beta)&=\frac{2}{\theta}\frac{1}{\sqrt{\tilde{\sigma}_0\tilde{\delta}}}z^S(\beta)\sinh\left(\frac{2}{\theta}\sqrt{\frac{\tilde{\sigma}_0}{\tilde{\delta}}}\beta\right),\\ C_2'(\beta)&=-\frac{2}{\theta}\frac{1}{\sqrt{\tilde{\sigma}_0\tilde{\delta}}}z^S(\beta)\cosh\left(\frac{2}{\theta}\sqrt{\frac{\tilde{\sigma}_0}{\tilde{\delta}}}\beta\right). \end{aligned} \tag{28}$$

Integrating the above equations, we arrive at the following expressions:

$$\begin{aligned} C_1(\beta^*)&=\frac{2}{\theta}\frac{1}{\sqrt{\tilde{\sigma}_0\tilde{\delta}}}\int_{\beta_1}^{\beta^*}z^S(\beta)\sinh\left(\frac{2}{\theta}\sqrt{\frac{\tilde{\sigma}_0}{\tilde{\delta}}}\beta\right)\mathrm{d}\beta+M_1,\\ C_2(\beta^*)&=-\frac{2}{\theta}\frac{1}{\sqrt{\tilde{\sigma}_0\tilde{\delta}}}\int_{\beta_1}^{\beta^*}z^S(\beta)\cosh\left(\frac{2}{\theta}\sqrt{\frac{\tilde{\sigma}_0}{\tilde{\delta}}}\beta\right)\mathrm{d}\beta+M_2, \end{aligned} \tag{29}$$

in which β^* is an argument of $C_1(\beta^*)$ and $C_2(\beta^*)$ that belong to the interval $[\beta_1,\,\beta_2]$.

Substituting Eq. (29) into Eq. (26) and using the tip condition of Eq. (5b), we get,

$$\begin{aligned} \frac{\mathrm{d}\omega^S(\beta^*)}{\mathrm{d}\beta^*}=&-\frac{4}{\theta^2\tilde{\delta}}\int_{\beta_1}^{\beta^*}z^S(\beta)\cosh\left[\frac{2}{\theta}\sqrt{\frac{\tilde{\sigma}_0}{\tilde{\delta}}}(\beta-\beta^*)\right]\mathrm{d}\beta+\\ &M_1\frac{2}{\theta}\sqrt{\frac{\tilde{\sigma}_0}{\tilde{\delta}}}\sinh\left(\frac{2}{\theta}\sqrt{\frac{\tilde{\sigma}_0}{\tilde{\delta}}}\beta^*\right)+M_2\frac{2}{\theta}\sqrt{\frac{\tilde{\sigma}_0}{\tilde{\delta}}}\cosh\left(\frac{2}{\theta}\sqrt{\frac{\tilde{\sigma}_0}{\tilde{\delta}}}\beta^*\right), \end{aligned} \tag{30}$$

where $\mathrm{d}\omega^S(\beta^*)/\mathrm{d}\beta^*=0$ when $\beta^*=\beta_1$ and β_2. The unknown coefficients M_1 and M_2 are,

therefore, obtained as,

$$\begin{aligned} M_1 &= \frac{2}{\theta\sqrt{\tilde{\sigma}_0\tilde{\delta}}}\frac{\cosh\left(\frac{2}{\theta}\sqrt{\frac{\tilde{\sigma}_0}{\tilde{\delta}}}\beta_1\right)}{\sinh\left(2\sqrt{\frac{\tilde{\sigma}_0}{\tilde{\delta}}}\right)}\int_{\beta_1}^{\beta_2} z^S(\beta)\cosh\left[\frac{2}{\theta}\sqrt{\frac{\tilde{\sigma}_0}{\tilde{\delta}}}(\beta-\beta_2)\right]\mathrm{d}\beta, \\ M_2 &= -\frac{2}{\theta\sqrt{\tilde{\sigma}_0\tilde{\delta}}}\frac{\sinh\left(\frac{2}{\theta}\sqrt{\frac{\tilde{\sigma}_0}{\tilde{\delta}}}\beta_1\right)}{\sinh\left(2\sqrt{\frac{\tilde{\sigma}_0}{\tilde{\delta}}}\right)}\int_{\beta_1}^{\beta_2} z^S(\beta)\cosh\left[\frac{2}{\theta}\sqrt{\frac{\tilde{\sigma}_0}{\tilde{\delta}}}(\beta-\beta_2)\right]\mathrm{d}\beta. \end{aligned} \tag{31}$$

Finally, we obtain the exact relations between ω^S and z^S as,

$$\begin{aligned} \omega^S(\beta^*) =& \frac{2}{\theta\sqrt{\tilde{\sigma}_0\tilde{\delta}}}\int_{\beta_1}^{\beta^*} z^S(\beta)\sinh\left(2\sqrt{\frac{\tilde{\sigma}_0}{\tilde{\delta}}}\frac{\beta-\beta^*}{\theta}\right)\mathrm{d}\beta + \\ & \frac{2}{\theta\sqrt{\tilde{\sigma}_0\tilde{\delta}}}\frac{\cosh\left(2\sqrt{\frac{\tilde{\sigma}_0}{\tilde{\delta}}}\frac{\beta^*-\beta_1}{\theta}\right)}{\sinh\left(2\sqrt{\frac{\tilde{\sigma}_0}{\tilde{\delta}}}\right)}\int_{\beta_1}^{\beta_2} z^S(\beta)\cosh\left(2\sqrt{\frac{\tilde{\sigma}_0}{\tilde{\delta}}}\frac{\beta-\beta_2}{\theta}\right)\mathrm{d}\beta, \end{aligned} \tag{32}$$

$$\begin{aligned} \frac{\mathrm{d}\omega^S(\beta^*)}{\mathrm{d}\beta^*} =& -\frac{4}{\theta^2\tilde{\delta}}\int_{\beta_1}^{\beta^*} z^S(\beta)\cosh\left[\frac{2}{\theta}\sqrt{\frac{\tilde{\sigma}_0}{\tilde{\delta}}}(\beta-\beta^*)\right]\mathrm{d}\beta + \\ & \frac{4\sinh\left[\frac{2}{\theta}\sqrt{\frac{\tilde{\sigma}_0}{\tilde{\delta}}}(\beta^*-\beta_1)\right]}{\theta^2\tilde{\delta}\sinh\left(2\sqrt{\frac{\tilde{\sigma}_0}{\tilde{\delta}}}\right)}\int_{\beta_1}^{\beta_2} z^S(\beta)\cosh\left[\frac{2}{\theta}\sqrt{\frac{\tilde{\sigma}_0}{\tilde{\delta}}}(\beta-\beta_2)\right]\mathrm{d}\beta. \end{aligned} \tag{33}$$

4.2.2. $\sigma_0 < 0$, $2\chi_S + \zeta_S > 0$

In this case, the general solution of Eq. (23) is given as,

$$\omega^S(\beta) = C_1(\beta)\cos\left(\frac{2}{\theta}\sqrt{-\frac{\tilde{\sigma}_0}{\tilde{\delta}}}\beta\right) + C_2(\beta)\sin\left(\frac{2}{\theta}\sqrt{-\frac{\tilde{\sigma}_0}{\tilde{\delta}}}\beta\right). \tag{34}$$

The functions $C_1(\beta)$, $C_2(\beta)$ can be determined in similar manner as in subsection 4.2.1. Here, we only list the resulting relations between z^S, ω^S, and its derivative. They are

$$\begin{aligned}\omega^S(\beta^*) =& \frac{2}{\theta\sqrt{-\tilde{\sigma}_0\tilde{\delta}}}\int_{\beta_1}^{\beta^*} z^S(\beta)\sin\left(2\sqrt{-\frac{\tilde{\sigma}_0}{\tilde{\delta}}}\frac{\beta-\beta^*}{\theta}\right)\mathrm{d}\beta- \\ & \frac{2}{\theta\sqrt{-\tilde{\sigma}_0\tilde{\delta}}}\frac{\cos\left(2\sqrt{-\frac{\tilde{\sigma}_0}{\tilde{\delta}}}\frac{\beta^*-\beta_1}{\theta}\right)}{\sin\left(2\sqrt{-\frac{\tilde{\sigma}_0}{\tilde{\delta}}}\right)}\int_{\beta_1}^{\beta_2} z^S(\beta)\cos\left(2\sqrt{-\frac{\tilde{\sigma}_0}{\tilde{\delta}}}\frac{\beta-\beta_2}{\theta}\right)\mathrm{d}\beta,\end{aligned} \tag{35}$$

and

$$\begin{aligned}\frac{\mathrm{d}\omega^S(\beta^*)}{\mathrm{d}\beta^*} =& -\frac{4}{\theta^2\tilde{\delta}}\int_{\beta_1}^{\beta^*} z^S(\beta)\cos\left(2\sqrt{-\frac{\tilde{\sigma}_0}{\tilde{\delta}}}\frac{\beta-\beta^*}{\theta}\right)\mathrm{d}\beta+ \\ & \frac{4}{\theta^2\tilde{\delta}}\frac{\sin\left(2\sqrt{-\frac{\tilde{\sigma}_0}{\tilde{\delta}}}\frac{\beta^*-\beta_1}{\theta}\right)}{\sin\left(2\sqrt{-\frac{\tilde{\sigma}_0}{\tilde{\delta}}}\right)}\int_{\beta_1}^{\beta_2} z^S(\beta)\cos\left(2\sqrt{-\frac{\tilde{\sigma}_0}{\tilde{\delta}}}\frac{\beta-\beta_2}{\theta}\right)\mathrm{d}\beta.\end{aligned} \tag{36}$$

4.2.3. $\sigma_0 = 0$, $2\chi_S + \zeta_S > 0$

In this case, by integrating Eq. (23), we get,

$$\frac{\mathrm{d}\omega^S(\beta^*)}{\mathrm{d}\beta^*} = -\frac{4}{\theta^2\tilde{\delta}}\int_{\beta_1}^{\beta^*} z^S(\beta)\mathrm{d}\beta + M_3. \tag{37}$$

For the tip condition of Eq. (5b) to be satisfied, we find that $M_3 = 0$ and

$$\int_{\beta_1}^{\beta_2} z^S(\beta)\mathrm{d}\beta = 0. \tag{38}$$

Therefore, $\omega^S(\beta^*)$ can be obtained by integrating Eq. (37) to arrive at,

$$\omega^S(\beta^*) = \frac{4}{\theta^2\tilde{\delta}}\int_{\beta_1}^{\beta^*}(\beta-\beta^*)z^S(\beta)\mathrm{d}\beta + M_4, \tag{39}$$

with an extra unknown constant M_4, to be determined by solving the system of Eqs. (24) and (25).

5. Numerical solution

Using the linear transformation

$$\beta = \frac{\theta}{2}\bar{\beta} + b, \tag{40}$$

in which $\theta/2$ is the coefficient of linear transformation and $b = (\beta_1 + \beta_2)/2$, the integrals involved in Eqs. (24) and (25) can be transformed to those over the interval $\bar{\beta} \in [-1, 1]$ in order to use established numerical quadratures. The transformed system of boundary integral equations is not presented here for the sake of brevity, it is obtained similarly to that for the Gurtin-Murdoch arc in Han et al. (2023).

5.1. Approximations of the unknown functions

On a circular arc, it is reasonable to approximate sufficiently smooth functions by truncated series of trigonometric functions. To account for the tip conditions of Eq. (5), we suggest to use the square root weight function, as in Mogilevskaya et al. (2021b), Zemlyanova et al. (2023), Han et al. (2023). Thus, the approximations for $\tilde{\sigma}^S(\beta)$ and $z^S(\beta)$ are taken as

$$\begin{aligned}\tilde{\sigma}^S(\bar{\beta}) = \sqrt{1-\bar{\beta}^2}\sum_{m=0}^{N} \{&A_m[\cos(2mt)\cos(mg) - \sin(2mt)\sin(mg)] + \\ &B_m[\sin(2mt)\cos(mg) + \cos(2mt)\sin(mg)]\},\end{aligned} \tag{41a}$$

$$\begin{aligned}z^S(\bar{\beta}) = \sqrt{1-\bar{\beta}^2}\sum_{m=0}^{N} \{&D_m[\cos(2mt)\cos(mg) - \sin(2mt)\sin(mg)] + \\ &E_m[\sin(2mt)\cos(mg) + \cos(2mt)\sin(mg)]\},\end{aligned} \tag{41b}$$

where A_m, B_m, D_m, and E_m are unknown coefficients for the m-th terms in truncated series and

$$t = t(\bar{\beta}) = \theta/4(\bar{\beta} - \bar{\beta}_0),\ \ g = g(\bar{\beta}_0) = \theta\bar{\beta}_0/2 + b, \tag{42}$$

where β_0 is the angle that corresponds to some point at the arc that in the following will be used as a collocation point, and $\bar{\beta}_0$ is obtained from β_0 using Eq. (40).

It is clear that the use of Eq. (41) allows for automatic satisfactions of the two tip conditions given by Eqs. (5a) and (5c). The remaining tip condition, Eq. (5b), can be used to determine the extra coefficients appearing in the relations between z^S and ω^S, such as e.g., constants M_1 and M_2 of Eq. (30).

5.2. Evaluation of the integrals

Substituting the approximations of Eq. (41) into the system of Eqs. (24), (25) and implementing the linear transformation of Eq. (40), we find that the right-hand side of Eqs. (24) and (25) contain the same six types of integrals as in Han et al. (2023), which are

$$
\begin{aligned}
I_1^m &= \int_{-1}^{1} \sqrt{1-\bar{\beta}^2}\cos(2mt)\mathrm{d}\bar{\beta}, \\
I_2^m &= \int_{-1}^{1} \sqrt{1-\bar{\beta}^2}\sin(2mt)\mathrm{d}\bar{\beta}, \\
I_3^m &= \int_{-1}^{1} \sqrt{1-\bar{\beta}^2}\frac{\sin(2mt)\sin 2t}{1-\cos(2t)}\mathrm{d}\bar{\beta} = \int_{-1}^{1} \sqrt{1-\bar{\beta}^2}\frac{\sin(2mt)}{\tan t}\mathrm{d}\bar{\beta}, \\
I_4^m &= \int_{-1}^{1} \sqrt{1-\bar{\beta}^2}\frac{\cos(2mt)}{1-\cos(2t)}\mathrm{d}\bar{\beta}, \\
I_5^m &= \int_{-1}^{1} \sqrt{1-\bar{\beta}^2}\frac{\sin(2mt)}{1-\cos(2t)}\mathrm{d}\bar{\beta}, \\
I_6^m &= \int_{-1}^{1} \sqrt{1-\bar{\beta}^2}\frac{\cos(2mt)\sin 2t}{1-\cos(2t)}\mathrm{d}\bar{\beta} = \int_{-1}^{1} \sqrt{1-\bar{\beta}^2}\frac{\cos(2mt)}{\tan t}\mathrm{d}\bar{\beta},
\end{aligned}
\tag{43}
$$

where the superscript m in I_i^m $(i = 1, \cdots, 6)$ denotes the integral related to the m-th term in the truncated series.

It can be easily seen that the integrals I_1^m and I_2^m of Eq. (43) are regular integrals, which can be evaluated by using the Gaussian quadrature. It was shown in Han et al. (2023) that I_3^m is also regular integral whose kernel reaches the limiting value of $2m\sqrt{1-\bar{\beta}^2}$ when $t \to 0$.

The singular integrals, I_4^m, I_5^m and I_6^m, can be evaluated as in Han et al. (2023). For the readers convenience we provide some details in Appendix.

The items on the left-hand side of Eqs. (24), (25) are different from the ones appearing in the corresponding problem for the Gurtin-Murdoch arc. This is especially true for ω^S that can be expressed via of z^S by one of Eqs. (32), (35), (39). However, those integrals are regular ones and can be accurately evaluated by the Gaussian quadrature. As in Han et al. (2023), we will use 800 Gaussian points to obtain accurate numerical results for regular integrals.

5.3. Reduction to linear system equations and post-processing

Standard collocation method is used to generate the system of linear algebraic equations from the governing integral equations of Eqs. (24), (25).

If the series in Eq. (41) are truncated at $m = N$, the total number of unknown coefficients in the approximations for $\tilde{\sigma}^S$ and z^S is $4(N + 1)$. To obtain these coefficients, $2(N + 1)$ collocation points are required. They are chosen to be uniformly distributed on the circular arc L away from its tips, since the approximations of Eq. (41) already satisfy the two tip conditions of Eq. (5).

It has been mentioned that in the case of $\sigma_0 = 0$ and $2\chi_S + \zeta_S > 0$, an extra unknown coefficient M_4 appears in Eq. (39). However, due to the fact that additional Eq. (38) for z^S is required for this case, the coefficient can be found together with all other coefficients from the solution of the system of $4(N + 1) + 1$ linear equations.

Substituting the approximations of Eq. (41) into the governing equations obtained from Eq. (24) and Eq. (25) by implementing linear transformation, and evaluating all integrals of Eq. (43) and those on left-hand side of Eqs. (32), (35), (39), we obtain the linear algebraic equations for each collocation point, similarly as Han et al. (2023).

After solving the system of such equations, one can obtain the coefficients A_m, B_m, D_m, E_m and M_4, if the case of $\tilde{\sigma}_0 = 0$ is considered. Substitution of those coefficients into the

approximations of Eq. (41) provides the values of $\tilde{\sigma}^S$ and z^S on the arc L, while the ω^S is evaluated via z^S using one of the three equations of Eqs. (32), (35) and (39).

The jumps $\Delta\tilde{\sigma} = \Delta\sigma/\mu = \Delta\tilde{\sigma}_n + \mathrm{i}\Delta\tilde{\sigma}_\ell$, needed for calculating stresses in the domain, can be then evaluated using Eqs. (2), (3). The corresponding dimensionless expressions are,

$$\begin{aligned} \Delta\tilde{\sigma}_n &= -\frac{\theta}{2}\tilde{\sigma}^S + \tilde{\sigma}_0\frac{\mathrm{d}\omega^S}{\mathrm{d}\bar{\beta}} - \tilde{\delta}\frac{\mathrm{d}^3\omega^S}{\mathrm{d}\bar{\beta}^3}, \\ \Delta\tilde{\sigma}_\ell &= \frac{\mathrm{d}}{\mathrm{d}\bar{\beta}}\tilde{\sigma}^S + \frac{\theta\tilde{\sigma}_0}{2}\omega^S - \frac{\theta\tilde{\delta}}{2}\frac{\mathrm{d}^2\omega^S}{\mathrm{d}\bar{\beta}^2}. \end{aligned} \tag{44}$$

The tractions $\sigma(z) = \sigma_n(z) + \mathrm{i}\sigma_\ell(z)$ outside of L are evaluated using Eq. (10), while the Cauchy stresses σ_{ij} are evaluated using Eq. (10) with the set of appropriately chosen normal vectors. For example, to calculate $\sigma_{11}(z)$ and $\sigma_{12}(z)$, one can set $z = \mathrm{i}x_2$ and assume that normal vector to the line on which z is located (axis Ox_2) points in Ox_1 direction. Thus, $\sigma_n(z) = \sigma_{11}(z)$ and $\sigma_\ell(z) = \sigma_{12}(z)$ on that line. Similarly, to obtain σ_{22}, one can set $z = x_1$ and assume that the normal to the line on which z is located (axis Ox_1) points in Ox_2 direction leading to $\sigma_{22} = \sigma_n$ on that line.

6. Comparison with the solution for the rigid circular arc problem

In Mogilevskaya et al. (2021b), it was shown that the problem of the Gurtin-Murdoch material surface (in plane strain setting) can be reduced to that of a rigid line (stiffener), if L is a straight segment and $\gamma = 0$, $\sigma_0 = 0$. However, in Han et al. (2023), we demonstrated that the plane strain problem of the Gurtin-Murdoch material surface is never reducible to that of a rigid curve, if L is a circular arc. We explained this using the classification of Benveniste and Miloh (2001) in which the Gurtin-Murdoch model with $\sigma_0 = 0$ represents different interface regime than that of rigid interface. The regime that corresponds to the Steigmann-Ogden model with $\sigma_0 = 0$ is also listed in Benveniste and Miloh (2001). So, we would like to compare the traction jumps for the Steigmann-Ogden model for that case with

the ones for the rigid arc that are reported in Liu and Jiang (1994).

As in Han et al. (2023), we consider the solutions of rigid arc for a special case of uniaxial load σ_{11}^{∞} for which $\varepsilon = 0$, see Eq. (62) in Liu and Jiang (1994), and take $\theta = \beta_2 - \beta_1 = \pi$. In that case, the following expression for the complex traction jump across the rigid arc is valid, see Han et al. (2023):

$$\Delta\sigma = -\frac{\kappa+1}{2\kappa}\frac{\sigma_{11}^{\infty}}{\sqrt{2\cos\beta}}\left[e^{-\mathrm{i}5\beta/2} + \frac{2\kappa^2-2\kappa-1}{2(2\kappa-1)}e^{\mathrm{i}\beta/2}\right]. \tag{45}$$

Therefore, the jumps in traction components across the rigid arc are,

$$\Delta\sigma_n = -\frac{\kappa+1}{2\kappa}\frac{\sigma_{11}^{\infty}}{\sqrt{2\cos\beta}}\left[\cos\left(\frac{5}{2}\beta\right) + \frac{2\kappa^2-2\kappa-1}{2(2\kappa-1)}\cos\left(\frac{\beta}{2}\right)\right], \tag{46a}$$

$$\Delta\sigma_\ell = \frac{\kappa+1}{2\kappa}\frac{\sigma_{11}^{\infty}}{\sqrt{2\cos\beta}}\left[\sin\left(\frac{5}{2}\beta\right) - \frac{2\kappa^2-2\kappa-1}{2(2\kappa-1)}\sin\left(\frac{\beta}{2}\right)\right]. \tag{46b}$$

We then take $\tilde{\sigma}_{11}^{\infty} = 1$, $\nu = 0.35$, $R = 1$, $\beta \in [-\pi/2, \pi/2]$ and compare the dimensionless jumps $\Delta\sigma_n/\mu$ and $\Delta\sigma_\ell/\mu$ obtained using Eq. (46) with the ones obtained with the Steigmann-Ogden model using Eq. (44). To do that, we assume $\sigma_0 = 0, \gamma = 0$, and vary the parameter $\tilde{\delta}$ as $\tilde{\delta} = 0.1$, 1, 10, 100. Note, that with the increase of $\tilde{\delta}$, the Steigmann-Ogden model describes a stiffer shell. The results of the comparison are presented on Fig. 2 together with the corresponding results for the Gurtin-Murdoch model, obtained in Han et al. (2023).

It can be seen from Fig. 2a that, for the case of $\sigma_0 = 0, \gamma = 0$, the normal traction jumps obtained with the Gurtin-Murdoch model are quite different from those for the rigid arc, while with the increase of $\tilde{\delta}$ (and the same values $\sigma_0 = 0, \gamma = 0$), the results with the Steigmann-Ogden model are closer to the rigid arc solutions when $\tilde{\delta} \geq 10$. It is also observed, see Fig. 2b, that the values of $\Delta\sigma_\ell/\mu$ for all three models (rigid arc, Gurtin-Murdoch, and Steigmann-Ogden) are very close and their magnitudes become very large

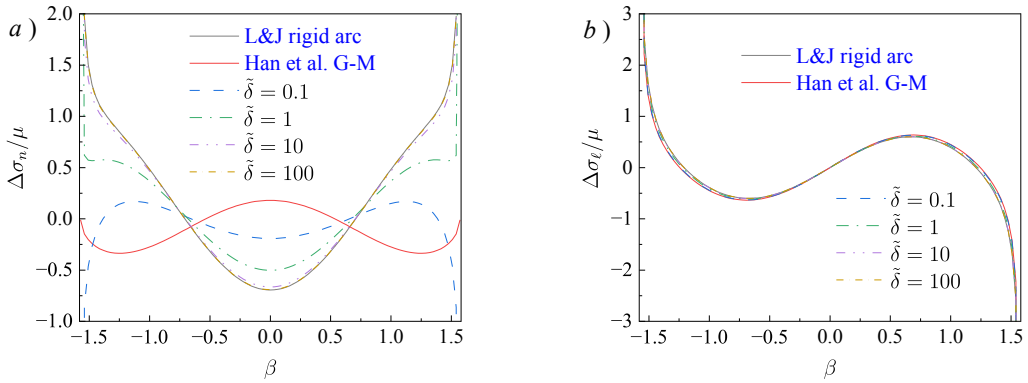

Figure 2: Comparisons of traction jumps $\Delta\sigma_n/\mu$ and $\Delta\sigma_\ell/\mu$ obtained using the Steigmann-Ogden model with the ones by Liu and Jiang (1994) and by Han et al. (2023).

when β is approaching β_1 and β_2. Here too, with the increase of $\tilde{\delta}$, the tangential traction jumps by Steigmann-Ogden model are closer to the rigid arc solutions than the ones by the Gurtin-Murdoch model.

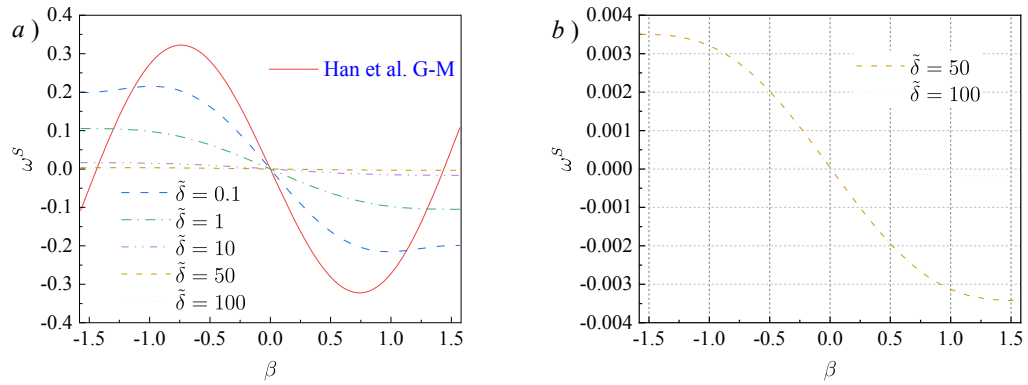

Figure 3: Comparisons of ω^S obtained using the Steigmann-Ogden and Gurtin-Murdoch models.

We also studied the variation of ω^S along the arc as the function of the parameter $\tilde{\delta}$, both for the Gurtin-Murdoch and Steigmann-Ogden models with $\sigma_0 = 0, \gamma = 0$. From Fig. 3, we can see that the plots of ω^S satisfy the boundary condition of Eq. (5b) for the Steigmann-Ogden model and the boundary condition of Eq. (6b) for the Gurtin-Murdoch model. From Fig. 3a, we find that with the increase of $\tilde{\delta}$ in Stegmann-Ogden, the absolute values of ω^S

decrease. However, from Fig. 3b, we can observe that the values of ω^S for $\tilde{\delta} = 50$ and 100 are still not constants.

7. Numerical results

We reiterate that all the results of this section are obtained, as in Han et al. (2023), using 800 Gaussian points to assure the accuracy. Also, the values of the kernels of all regular integrals involved in Eq. (43) are evaluated using Taylor series expansions when $|\bar{\beta} - \bar{\beta}_0| \leq 0.1$, in order to avoid near singularity.

7.1. Convergence analysis and influence of θ

Consider the following cases of arcs: (i) short arc ($\beta_1 = 89\pi/180$, $\beta_2 = 91\pi/180$), (ii) medium arc ($\beta_1 = \pi/4$, $\beta_2 = 3\pi/4$), and (iii) long arc ($\beta_1 = 0$, $\beta_2 = \pi$), all with the radius $R = 1$nm. We investigate the behavior of the approximations of Eq. (41) as functions of the truncation number m and study the influence of arc length θ on the results.

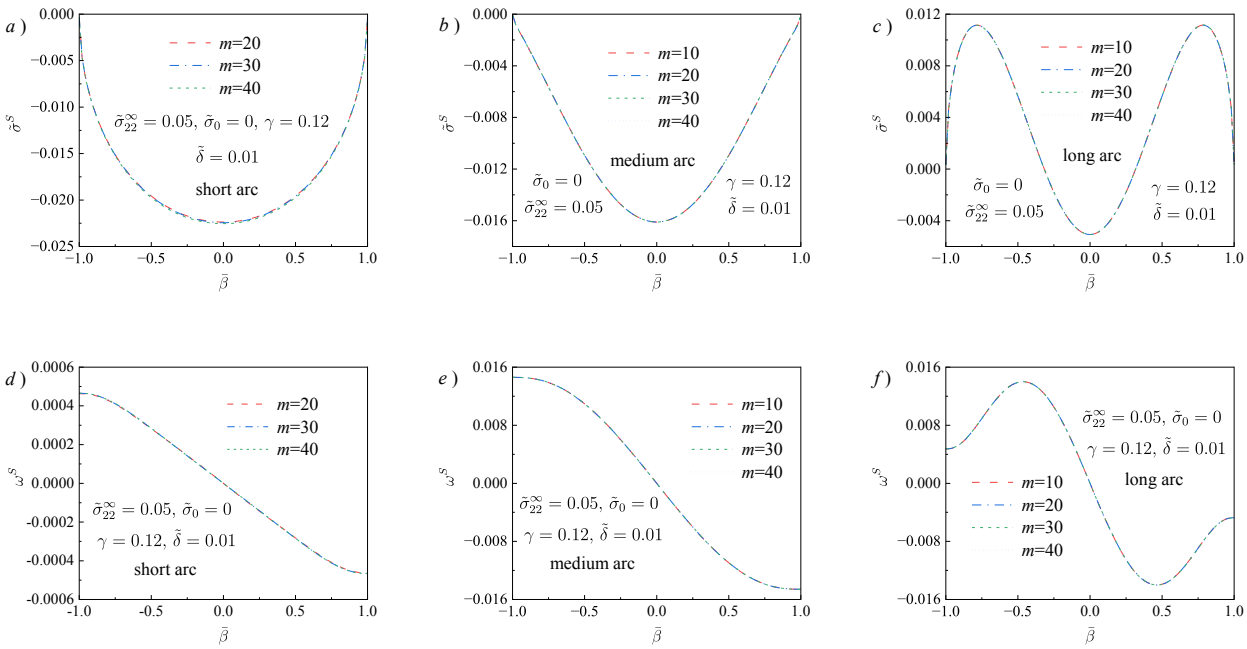

Figure 4: Distributions of $\tilde{\sigma}^S$ and ω^S as functions of m for the three types of arcs.

We set $\tilde{\sigma}_{22}^{\infty} = 0.05$, $\tilde{\sigma}_{11}^{\infty} = \tilde{\sigma}_{12}^{\infty} = 0$, $\nu = 0.33$ and take $\tilde{\sigma}_0 = 0$, $\tilde{\delta} = 0.01$, $\gamma = 0.12$, which is within the range of the parameters described in Zemlyanova et al. (2023) and in the references therein. The results of the convergence study are shown on Fig. 4 from which we find that, in the cases of medium and long arcs, the results for both $\tilde{\sigma}^S$ and ω^S converge at $m \geq 10$.

However, for the short arc, $\tilde{\sigma}^S$ and ω^S are convergent only when $m \geq 20$. Analyzing behavior of $\tilde{\sigma}^S$ from Fig. 4, we find that all the results satisfy the tip condition of Eq. (5a). Similarly, it can be seen that the results for ω^S satisfy the tip condition of Eq. (5b).

We also investigated the convergence behavior of the dimensionless traction jumps. From Eq. (44), one can see that, if $\tilde{\sigma}_0 = 0$, $\Delta\tilde{\sigma}_n$ is expressed via the combination of $\tilde{\sigma}^S$ and $\mathrm{d}^3\omega^S/\mathrm{d}\bar{\beta}^3$, while $\Delta\tilde{\sigma}_\ell$ via that of $\mathrm{d}\tilde{\sigma}^S/\mathrm{d}\bar{\beta}$ and $\mathrm{d}^2\omega^S/\mathrm{d}\bar{\beta}^2$. This explains dramatic variations of $\Delta\tilde{\sigma}_n$ and $\Delta\tilde{\sigma}_\ell$ near the tips, as can be seen from the plots of Fig. 5. From that figure, it can be concluded that taking the truncation number to be $m = 40$ is sufficient for the convergence of the results for the dimensionless traction jumps. Therefore, in the following numerical examples, we will set truncation number $m = 40$ in order to ensure accuracy.

From the above figures, we could also see that the arc length θ plays an important role on the distributions of the fields at and across the arc. From Fig. 4a, b, we find that the values of $\tilde{\sigma}^S$ at arcs (i) and (ii) are negative and, for both arcs, there exists a single minimum of $\tilde{\sigma}^S$ at $\bar{\beta} = 0$. The corresponding results for arc (iii) on Fig. 4c include both negative and positive values. In addition, the plot of $\tilde{\sigma}^S$ has three local extrema: maximum values of $\tilde{\sigma}^S = 0.011$ are reached at $\bar{\beta} = \pm 0.78$ and its minimum value of $\tilde{\sigma}^S = -0.0051$ is reached at $\bar{\beta} = 0$. From Fig. 4d, e, it can be seen that, for the arcs (i) and (ii), the maximum and minimum values of ω^S are reached at the tips and, with the increase of θ, the absolute values of ω^S increase. However, for arc (iii), the variation of ω^S is more dramatic, and the maximum absolute values of $\omega^S = 0.014$ occur at new points of extrema $\bar{\beta} = \pm 0.46$.

From Fig. 5, it can be seen that the influence of θ on $\Delta\tilde{\sigma}_n$ and $\Delta\tilde{\sigma}_\ell$ is even more

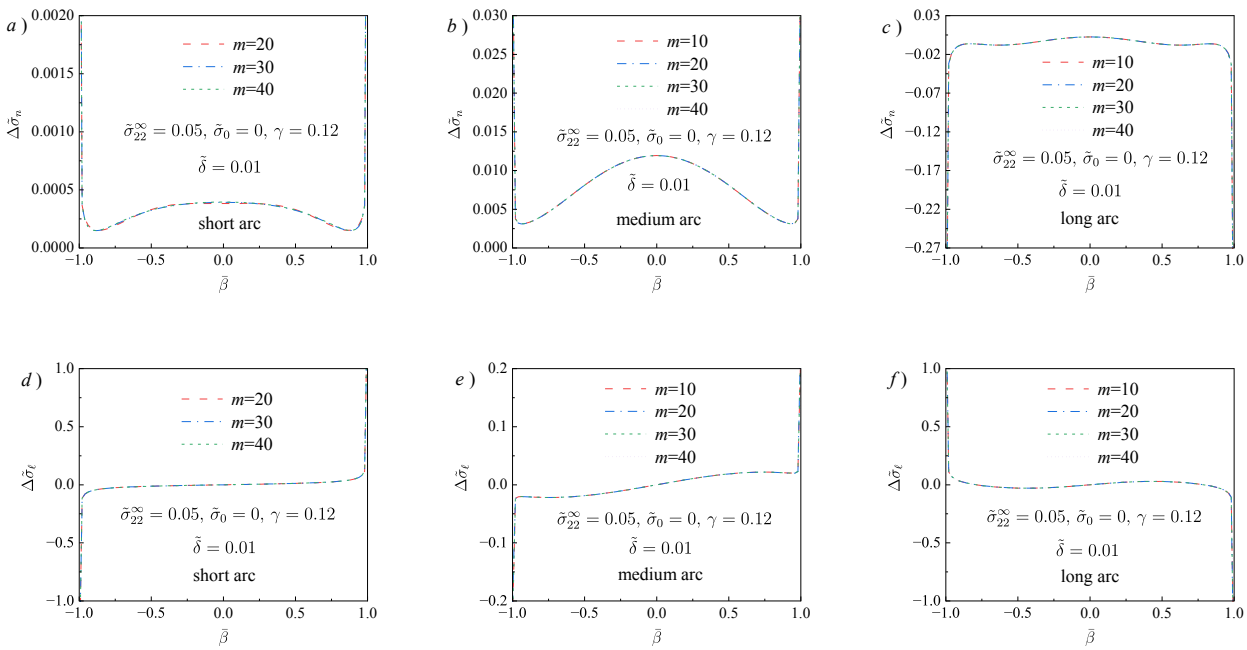

Figure 5: Distributions of $\Delta\tilde{\sigma}_n$ and $\Delta\tilde{\sigma}_\ell$ as functions of m for the three types of arcs.

pronounced than its influence on $\tilde{\sigma}^S$ and ω^S. We can see from Fig. 5a, b that, for the cases of arcs (i) and (ii), the maximum absolute values of $\Delta\tilde{\sigma}_n$ significantly increase with the increase of θ. However, the behavior of $\Delta\tilde{\sigma}_n$ for the case of arc (iii), shown in Fig. 5c, is completely reversed, as compared with that shown on Fig. 5a, b. From Fig. 5d, e, f, we find that the interval of variation of $\Delta\tilde{\sigma}_\ell$ first decreases as θ increases from case (i) to case (ii), but, for case (iii), this interval restores to the interval of variation for case (i) but the behavior of the plot for the latter case is completely reversed as compared to that for arc (i).

7.2. Influence of γ

We will study the influence of γ for the case of arc (iii) by taking $\gamma = 0.1,\ 1,\ 10,\ 100,\ 1000$. The rest of the parameters are chosen as $\tilde{\sigma}_{22}^{\infty} = 0.05$, $\tilde{\sigma}_{11}^{\infty} = \tilde{\sigma}_{12}^{\infty} = 0$, $\nu = 0.33$, $\tilde{\sigma}_0 = 0.025$, $\tilde{\delta} = 0.1$. The truncation number is still taken to be $m = 40$.

The distributions of $\tilde{\sigma}^S$ and ω^S for different γ are plotted on Fig. 6, from which we

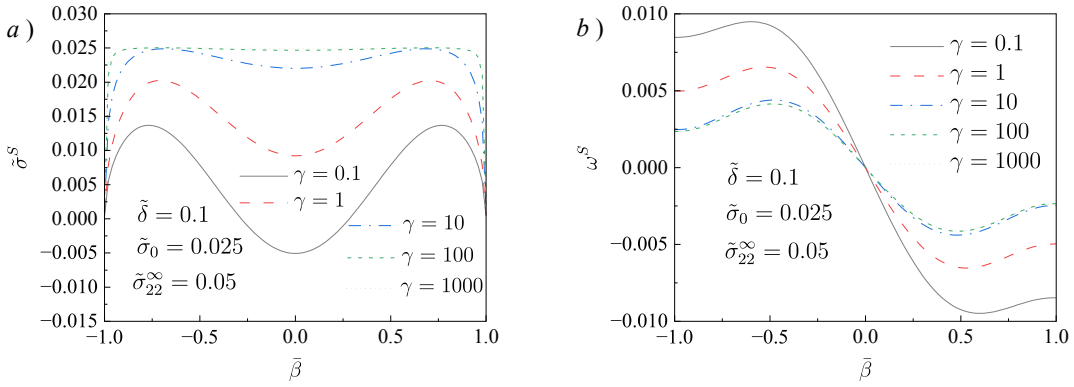

Figure 6: Distributions of $\tilde{\sigma}^S$ and ω^S along the long arc as functions of γ.

find that, with the increase of γ, the maximum values of $\tilde{\sigma}^S$ increase as they should, as $\tilde{\sigma}^S \to \tilde{\sigma}_0 = 0.025$ when $\gamma \to \infty$, while the plots $\tilde{\sigma}^S$ (apart from near tips regions) become flatter. On the contrary, the maximum values of ω^S decrease with the increase of γ and the plots start to converge to one another for $\gamma \geq 100$. From Fig. 6a, it is clear that $\tilde{\sigma}^S$ satisfies the tip condition of Eq. (5a) while it is also clear from Fig. 6b that ω^S satisfies the tip condition of Eq. (5b) at $\bar{\beta} = \pm 1$.

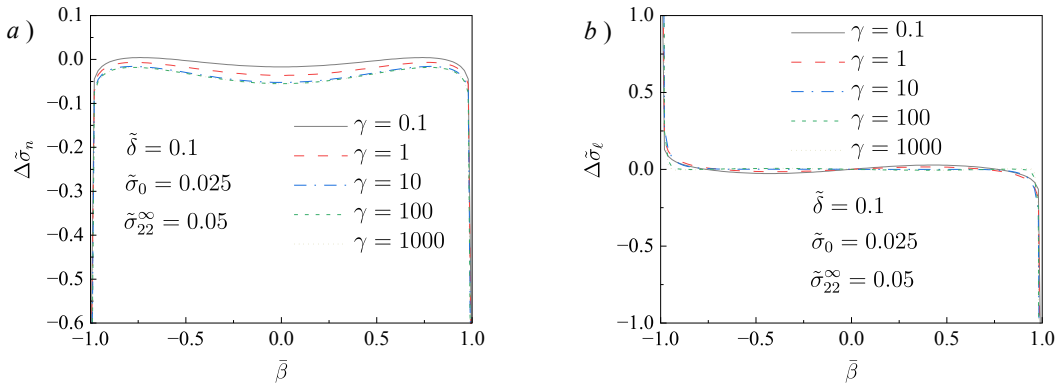

Figure 7: Distributions of $\Delta\tilde{\sigma}_n$ and $\Delta\tilde{\sigma}_\ell$ along the long arc as functions of γ.

We also investigated influence of γ on the distributions of $\Delta\tilde{\sigma}_n$ and $\Delta\tilde{\sigma}_\ell$. The results are shown in Fig. 7. From that figure, we find that $\Delta\tilde{\sigma}_n$ and $\Delta\tilde{\sigma}_\ell$ are close to zero almost

everywhere, except for the near-tip regions, where dramatic variations exist, due to the derivatives involved in Eq. (44). Both $\Delta\tilde{\sigma}_n$ and $\Delta\tilde{\sigma}_\ell$ reach some limit values for $\gamma \geq 100$. From Fig. 6a, we find that, with increase of γ, the change in $\tilde{\sigma}^S$ near the tips occur more rapidly leading to larger values of derivative $\mathrm{d}\tilde{\sigma}^S/\mathrm{d}\bar{\beta}$ in those regions. According to Eq. (44), it is expected that the maximum absolute values of $\Delta\tilde{\sigma}_\ell$ are increasing with increase of γ, which can be seen from Fig. 7b.

7.3. Influences of $\tilde{\sigma}_0$ and $\tilde{\delta}$

It was shown in Sections 4.2.1 - 4.2.2 that the solution of the problem under study might depend on the relationships between surface tension $\tilde{\sigma}_0$ and bending parameter $\tilde{\delta}$. From Eqs. (32) and (35), we find that those parameters come in combinations, such as $\sqrt{\pm\tilde{\sigma}_0/\tilde{\delta}}$ and $\sqrt{\pm\tilde{\sigma}_0\tilde{\delta}}$, where $\tilde{\sigma}_0$ might be positive or negative. Only when $\tilde{\sigma}_0 = 0$, as in Eq. (39), $\tilde{\delta}$ remains the only parameter influencing the numerical results.

We will consider case (ii) of medium arc and take $\tilde{\delta} = 0.1, 0.3$. To cover all three cases discussed in Sections 4.2.1 - 4.2.3, we choose $\tilde{\sigma}_0 = -0.025, 0, 0.025$. The rest of the parameters are set as $\tilde{\sigma}^\infty_{22} = 0.05$, $\tilde{\sigma}^\infty_{11} = \tilde{\sigma}^\infty_{12} = 0$, $\nu = 0.33, \gamma = 0.12$. The distributions of $\tilde{\sigma}^S$ and ω^S along the arc are shown on Fig. 8. Fig. 8a shows that, with the increase of $\tilde{\sigma}_0$ and constant $\tilde{\delta}$, the absolute values of $\tilde{\sigma}^S$ decrease, while with the increase of $\tilde{\delta}$, the absolute values of $\tilde{\sigma}^S$ increase. Fig. 8b shows that, with the increase of both $\tilde{\sigma}_0$ and $\tilde{\delta}$, the absolute values of ω^S decrease. Due to symmetry of the geometry and remote load, $\tilde{\sigma}^S$ is symmetric in respect to x_2-axis, while ω^S is anti-symmetric.

From Fig. 9a, we conclude that, for the various values of $\tilde{\sigma}_0$ and $\tilde{\delta}$, the jump $\Delta\tilde{\sigma}_n$ is close to zero for most values of $\bar{\beta}$, except near the tips, where the first and third order derivatives of ω^S involved in Eq. $(44)_1$ is the reason for the drastic variations. From Fig. 9b, we find that the $\Delta\tilde{\sigma}_\ell$ for $\tilde{\sigma}_0 = 0.025$ is of opposite sign than $\Delta\tilde{\sigma}_\ell$ for $\tilde{\sigma}_0 = -0.025$ and $\tilde{\sigma}_0 = 0$. In addition, $\Delta\tilde{\sigma}_n$ is symmetric and $\Delta\tilde{\sigma}_\ell$ is anti-symmetric.

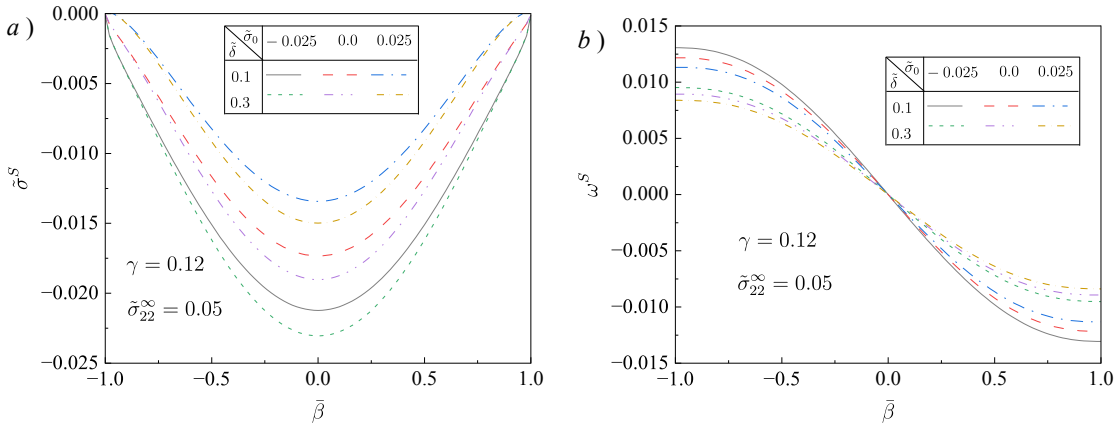

Figure 8: Distributions of $\tilde{\sigma}^S$ and ω^S along the medium arc as functions of $\tilde{\sigma}_0$ and $\tilde{\delta}$.

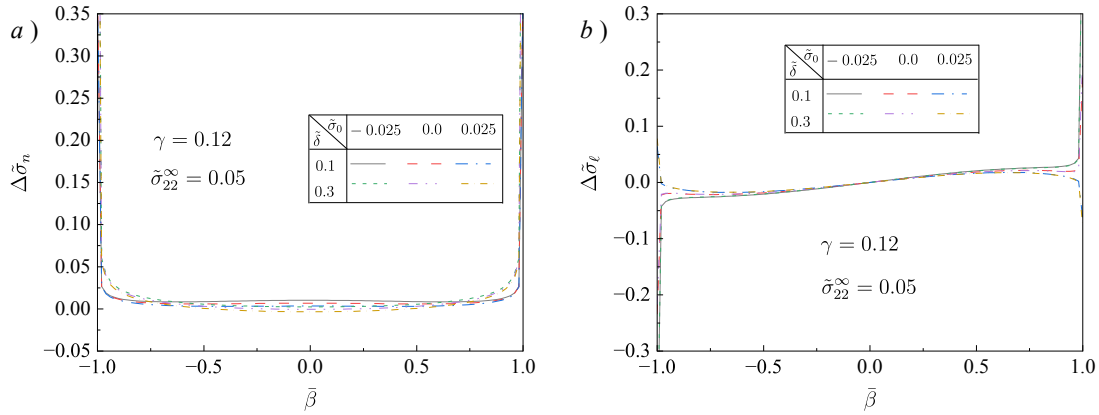

Figure 9: Distributions of $\Delta\tilde{\sigma}_n$ and $\Delta\tilde{\sigma}_\ell$ along the medium arc as functions of $\tilde{\sigma}_0$ and $\tilde{\delta}$.

7.4. Modeling of local fields in the bulk

We consider epoxy matrix with $\mu = 2$ GPa, $\nu = 0.35$ containing the material surface with circular arc cross-section characterized by $R = 5$ nm and $\beta_1 = \pi/4$, $\beta_2 = 3\pi/4$. The two-dimensional elastic properties of the arc are chosen to be equal to those reported in Suk et al. (2010) for graphene oxide, which results in the following dimensionless parameters: $\gamma = 0.12$ and $\tilde{\sigma}_0 = 0.025$. The bending parameter is set as $\tilde{\delta} = 0.2$. We assume, as in Mogilevskaya et al. (2008), that the only non-zero component of the far-field is $\sigma_{22}^{\infty} = 100$ MPa, which results in $\tilde{\sigma}_{22}^{\infty} = \sigma_{22}^{\infty}/\mu = 0.05$. The contours of the dimensionless Cauchy

stresses $\tilde{\sigma}_{ij}$ in the domain $x_1 \otimes x_2 \in [-6.5, 6.5] \otimes [-1.25, 8.5]$ (nm) are plotted on Fig. 10 and compared with those for the Gurtin-Murdoch model obtained in Han et al. (2023). On the figures, the same scale for each $\tilde{\sigma}_{ij}$ is used to allow for comparison.

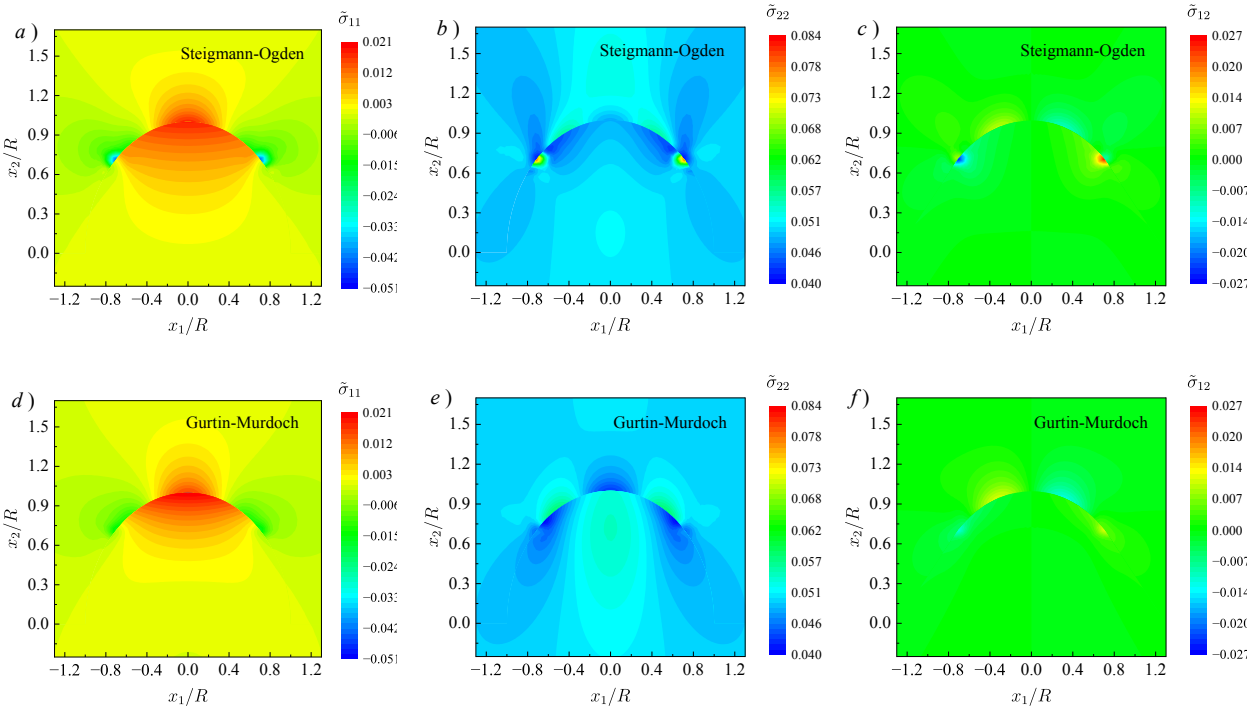

Figure 10: Contour plots of the dimensionless Cauchy stresses for the Steigmann-Ogden and Gurtin-Murdoch models.

It can be clearly seen from Fig. 10 that, for both models, all components $\tilde{\sigma}_{ij}$ undergo jumps across the arc. It is found that the symmetric properties of the plots due to the two models are the same; the distributions of $\tilde{\sigma}_{11}$ and $\tilde{\sigma}_{22}$ on Figs. 10a, b, d, e are symmetric with respect to x_2-axis, while the distribution of $\tilde{\sigma}_{12}$ is anti-symmetric from Fig. 10c, f. It also can be seen that the stress fields are not symmetric with respect to x_1-axis, unlike in the case of a straight segment, see Mogilevskaya et al. (2021b) .

From Fig. 10a, d, it can be observed that, for both models, $\tilde{\sigma}_{11}$ is tensile above and below the arc and it is compressive in the regions near the tips. The absolute values of $\tilde{\sigma}_{11}$ near the tips are larger for the Steigmann-Ogden model than for the Gurtin-Murdoch one. From

Fig. 10b, e, it can be concluded that, for both models, $\tilde{\sigma}_{22}$ is tensile everywhere in the region of interest. The differences in contour plots for the two models are more pronounced (which should be expected for the chosen far-field load) and here too $\tilde{\sigma}_{22}$ at the tips are larger in the case of the Steigmann-Ogden model. It is seen from Fig. 10c, f that $\tilde{\sigma}_{12}$ along the arc is anti-symmetric and again higher values of singular stresses at the tips are observed for the Steigmann-Ogden model.

We also compared the distributions of $\tilde{\sigma}^S$ and ω^S, $\Delta\tilde{\sigma}_n$, $\Delta\tilde{\sigma}_\ell$ for the both models.

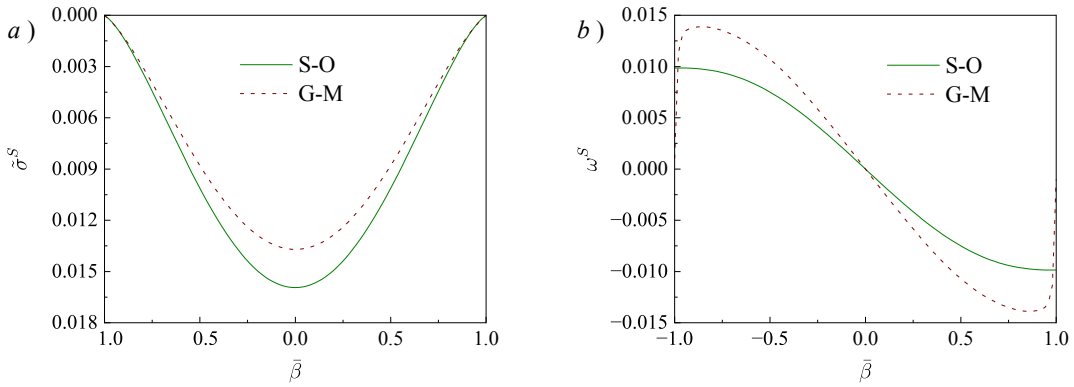

Figure 11: Comparison of distributions of $\tilde{\sigma}^S$ and ω^S obtained with the Steigmann-Ogden and Gurtin-Murdoch models.

From Fig. 11 we find that the maximum absolute values of $\tilde{\sigma}^S$ for the Gurtin-Murdoch model are smaller than for the Steigmann-Ogden model, while it is opposite for ω^S. It can clearly be seen from Fig. 11a that, for both Steigmann-Ogden and Gurtin-Murdoch models, $\tilde{\sigma}^S$ satisfies the tip conditions of Eqs. (5a) and (6a), while ω^S satisfies the respective tip conditions of Eqs. (5b) and (6b).

Fig. 12 indicate that traction jumps for both models are mostly affected near tip regions. The values $\Delta\tilde{\sigma}_n$ for the Steigmann-Ogden model are significant larger than for the Gurtin-Murdoch one, while the values of $\Delta\tilde{\sigma}_\ell$ for the Gurtin-Murdoch model are slightly larger than for the Steigmann-Ogden model. Retrospect the singularities shown on Fig. 10, we can conclude that the $\Delta\tilde{\sigma}_n$ plays a more significant role than $\Delta\tilde{\sigma}_\ell$ in determining tip singularities.

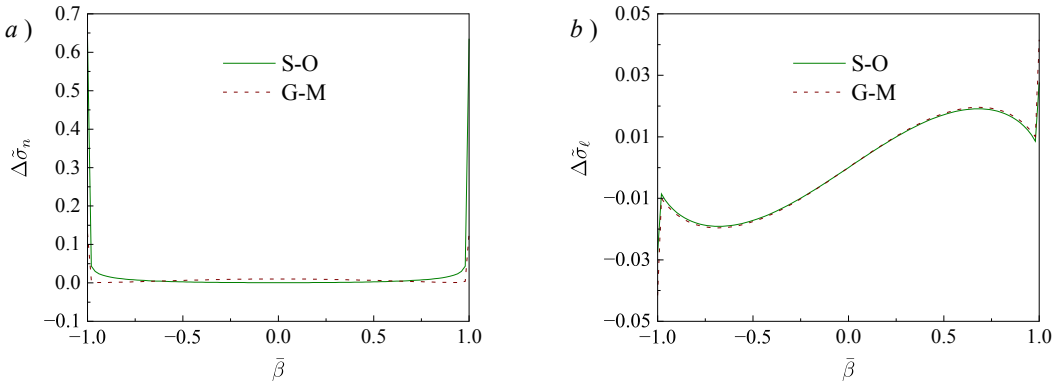

Figure 12: Comparison of of distributions of $\Delta\tilde{\sigma}_n$ and $\Delta\tilde{\sigma}_\ell$ obtained with the Steigmann-Ogden and Gurtin-Murdoch models.

8. Conclusions

In this paper, we derived the solution for the plane strain problem of an infinite isotropic elastic matrix subjected to uniform far-field load and containing a Steigmann-Ogden material surface of circular cross-section. The solution allows for accurate evaluations of all elastic fields everywhere in the material system. We demonstrated that, as in the corresponding problem with a Gurtin-Murdoch material surface, the equations for the components of the surface stress tensor are fully coupled for the case on nonzero surface tension (unlike for the straight segment case considered in Mogilevskaya et al. (2021b)). We investigated the influence of the dimensionless parameters that govern the problem. For the case of zero surface tension, we compared our solution with that for the corresponding problem involving a rigid arc, by choosing special values for the governing parameters and found that the results obtained with the Steigmann-Ogden model with decreasing elastic and bending parameters are closer to those for the rigid arc. However, we emphasize again that, when the surface tension vanishes, the two models represent two different interface regimes of seven regimes listed in Benveniste and Miloh (2001). The obtained solution can be used as a benchmark example for the numerical solutions of the problems involving surfaces of arbitrary suffi-

ciently smooth shapes, that is a subject of our future work, which will also include solving more complex three-dimensional problems.

Acknowledgments

Zhilin Han gratefully acknowledges support from the National Natural Science Foundation of China through NSFC No. 12002084. Anna Y. Zemlyanova gratefully acknowledges the support from the Simons Collaboration Grant for Mathematicians (2020-2025), award number 713080. Sofia G. Mogilevskaya gratefully acknowledges the support from the National Science Foundation, United States, award number NSF CMMI-2112894. The second (A. Z.) and third (S. M.) authors would like to thank the Isaac Newton Institute for Mathematical Sciences, Cambridge, for support and hospitality during the programme CATW04 where the part of work on this paper was undertaken. This part was supported by EPSRC grant no EP/R014604/1.

Appendix

We will explain the technique of evaluation of singular integrals using I_4^m as an example. This integral can be represented as follows:

$$I_4^m = \int_{-1}^{1} \sqrt{1-\bar{\beta}^2}\left[\frac{\cos(2mt)}{1-\cos(2t)} - \frac{1}{2t^2}\right] \mathrm{d}\bar{\beta} + \frac{1}{2} \Xint= _{-1}^{1} \frac{\sqrt{1-\bar{\beta}^2}}{t^2} \mathrm{d}\bar{\beta}, \tag{47}$$

As $t \to 0$, the kernel of the first integral on the right hand-side of Eq. (47) reaches the value of $\sqrt{1-\bar{\beta}^2}\,(-m^2+1/6)$. Therefore, this integral is a regular one and can be numerically evaluated by using the Gaussian quadrature. The second integral on the right hand-side of Eq. (47) is hypersingular integral, which can analytically be evaluated as, see Lin'kov and Mogilevskaya (1990), Martin (1992),

$$\Xint= _{-1}^{1} \frac{\sqrt{1-\bar{\beta}^2}}{t^2} \mathrm{d}\bar{\beta} = \Xint= _{-1}^{1} \frac{\sqrt{1-\bar{\beta}^2}}{\left[\theta/4(\bar{\beta}-\bar{\beta}_0)\right]^2} \mathrm{d}\bar{\beta} = \frac{16}{\theta^2} \Xint= \frac{\sqrt{1-\bar{\beta}^2}}{\left(\bar{\beta}-\bar{\beta}_0\right)^2} \mathrm{d}\bar{\beta} = -\frac{16}{\theta^2}\pi. \tag{48}$$

I_5^m and I_6^m can be similarly evaluated by representing them as,

$$\begin{aligned} I_5^m &= \int_{-1}^{1} \sqrt{1-\bar{\beta}^2} \left[\frac{\sin(2mt)}{1-\cos(2t)} - \frac{m}{t} \right] \mathrm{d}\bar{\beta} + m \fint_{-1}^{1} \frac{\sqrt{1-\bar{\beta}^2}}{t} \mathrm{d}\bar{\beta}, \\ I_6^m &= \int_{-1}^{1} \sqrt{1-\bar{\beta}^2} \left[\frac{\cos(2mt)}{\tan t} - \frac{1}{t} \right] \mathrm{d}\bar{\beta} + \fint_{-1}^{1} \frac{\sqrt{1-\bar{\beta}^2}}{t} \mathrm{d}\bar{\beta}. \end{aligned} \tag{49}$$

The first integrals of Eqs. (49) are again regular integrals that can be evaluated by using the Gaussian quadrature, while the second integral involved in both expressions of Eq. (49) is the Cauchy principal value integral, which can be evaluated analytically as, see Martin (1992),

$$\fint_{-1}^{1} \frac{\sqrt{1-\bar{\beta}^2}}{t} \mathrm{d}\bar{\beta} = \fint_{-1}^{1} \frac{\sqrt{1-\bar{\beta}^2}}{\theta/4(\bar{\beta}-\bar{\beta}_0)} \mathrm{d}\bar{\beta} = \frac{4}{\theta} \fint \frac{\sqrt{1-\bar{\beta}^2}}{\bar{\beta}-\bar{\beta}_0} \mathrm{d}\bar{\beta} = -\frac{4}{\theta} \bar{\beta}_0 \pi. \tag{50}$$

References

Ballarini, R. (1987). An integral equation approach for rigid line inhomogeneity problems. *Int. J. Fract.*, 33:R23–R26. 1

Baranova, S., Mogilevskaya, S., Mantic, V., and Jiménez-Alfaro, S. (2020). Analysis of the antiplane problem with an embedded zero thickness layer described by the Gurtin-Murdoch model. *J. Elast.*, 140:171–195. 1

Benveniste, Y. and Miloh, T. (2001). Imperfect soft and stiff interfaces in two-dimensional elasticity. *Mech. Mater.*, 33:309–323. 2, 6, 8

Cao, G. (2014). Atomistic studies of mechanical properties of graphene. *Polymers*, 6:2404–2432. 1

Corso, F. D., Bigoni, D., and Gei, M. (2008). The stress concentration near a rigid line inclusion in a prestressed, elastic material. Part I. Full field solution and asymptotics. *J. Mech. Phys. Solids*, 56:815–838. 1

Goudarzi, M., Corso, F. D., Bigoni, D., and Simone, A. (2020). Dispersion of rigid line inclusions as stiffeners and shear band instability triggers. *Int. J. Solids Struct.* 1

Güler, O. and Bağcı, N. (2020). A short review on mechanical properties of graphene reinforced metal matrix composites. *J. Mater. Res. Technol.*, 9:6808–6833. 1

Gurtin, M. and Murdoch, A. (1975). A continuum theory of elastic material surfaces. *Arch. Ration. Mech. Anal.*, 57:291–323. 1

Gurtin, M. and Murdoch, A. (1978). Surface stress in solids. *Int. J. Solids Struct.*, 14:431–440. 1

Han, Z., Mogilevskaya, S., and Zemlyanova, A. (2023). On the problem of a gurtin-murdoch cylindrical material surface embedded in an infinite matrix. *Int.J.Solids Struct.* 1, 2, 2, 3, 3, 3, 5, 5.1, 5.2, 5.2, 5.3, 6, 6, 2, 7, 7.4

Lin'kov, A. and Mogilevskaya, S. (1990). Hypersingular integrals in plane problems of the theory of elasticity. *PMM-J. Appl. Math. Mech.*, 54(1):93–99. 8

Linkov, A. and Mogilevskaya, S. (1998). Complex hypersingular BEM in plane elasticity problems. *In: Sladek, V., Sladek, J. (Eds.), Singular Integrals in Boundary Element Method, Chapter 9. Computational Mechanics Publication*, pages 299–364. 3

Liu, Y. and Jiang, C. (1994). Stress distribution at the rigid circular arc inclusion end. *Eng. Fract. Mech.*, 47(3):431–440. 1, 6, 2

Markenscoff, X., Ni, L., and Dundurs, J. (1994). The interface anticrack and Green's functions for interacting anticracks and cracks/anticracks. *J. Appl. Mech.*, 61(4):797–802. 1

Martin, P. (1992). Exact solution of a simple hypersingular integral equation. *J. Integral Equ. Appl.*, pages 197–204. 8, 8

Mirzaei, M. and Abbasi, M. (2023). Dynamic response of moderately thick graphene reinforced composite cylindrical panels under the action of moving load. *Eng. Anal. Bound. Elem.*, 146:292–305. 1

Mogilevskaya, S., Crouch, S., and Stolarski, H. (2008). Multiple interacting circular nano-inhomogeneities with surface/interface effects. *J. Mech. Phys. Solids*, 56:2928–2327. 7.4

Mogilevskaya, S. and Linkov, A. (1998). Complex fundamental solutions and complex variables boundary element method in elasticity. *Comput. Mech.*, 22:88–92. 3

Mogilevskaya, S., Zemlyanova, A., and Kushch, V. (2021a). Fiber- and particle-reinforced composite materials with the Gurtin–Murdoch and Steigmann–Ogden surface energy endowed interfaces. *Appl. Mech. Rev.*, 73(5). 2, 3

Mogilevskaya, S., Zemlyanova, A., and Mantič, V. (2021b). The use of the Gurtin-Murdoch theory for modeling mechanical processes in composites with two-dimensional reinforcements. *Compos. Sci. Technol.*, 210:108751. 1, 2, 2, 3, 3, 3, 5.1, 6, 7.4, 8

Papageorgiou, D., Kinloch, I., and Young, R. (2017). Mechanical properties of graphene and graphene-based nanocomposites. *Prog. Mater. Sci.*, 90:75–127. 1

Papageorgiou, D., Li, Z., Liu, M., Kinloch, I., and Young, R. (2020). Mechanisms of mechanical reinforcement by graphene and carbon nanotubes in polymer nanocomposites. *Nanoscale*, 12:2228–2267. 1

Steigmann, D. and Ogden, R. (1997). Plain deformations of elastic solids with intrinsic boundary elasticity. *Proc. R. Soc. London A*, 453:853–877. 1

Steigmann, D. and Ogden, R. (1999). Elastic surface-substrate interactions. *Proceedings of the Royal Society of London. Series A: Mathematical, Physical and Engineering Sciences*, 455(1982):437–474. 1

Suk, J., Piner, R., An, J., and Ruoff, R. (2010). Mechanical properties of monolayer graphene oxide. *ACS Nano*, 4:6557–6564. 1, 7.4

Wang, Z., Zhang, H., and Chou, Y. (1985). Characteristics of the elastic field of a rigid line inhomogeneity. *J. Appl. Mech.*, 52:818–822. 1

Zemlyanova, A. Y. (2023). A problem for a material surface attached to the boundary of an elastic semiplane. *Math. Mech. Solids*, page 10812865231184415. 1

Zemlyanova, A. Y., Mogilevskaya, S. G., and Schillinger, D. (2023). Numerical solution of the two-dimensional steigmann–ogden model of material surface with a boundary. *Physica D*, 443(133531). 1, 2, 2, 3, 3, 3, 5.1, 7.1